

Multi-messenger Emission from Tidal Waves in Neutron Star Oceans

Andrew G. Sullivan,^{1*} Lucas M. B. Alves,¹ Georgina O. Spence,² Isabella P. Leite,³
Doğa Veske,¹ Imre Bartos,⁴ Zsuzsa Márka,⁵ Szabolcs Márka¹

¹*Department of Physics, Columbia University in the City of New York, New York, NY 10027, USA*

²*Department of Mathematics, Barnard College of Columbia University in the City of New York, New York, NY 10027, USA*

³*Department of Biomedical Engineering, Columbia University in the City of New York, New York, NY 10027, USA*

⁴*Department of Physics, University of Florida, Gainesville, FL 32611-8440, USA*

⁵*Columbia Astrophysics Laboratory, Columbia University in the City of New York, New York, NY 10027, USA*

Accepted XXX. Received YYY; in original form ZZZ

ABSTRACT

Astrophysical binary systems including neutron stars represent exciting sources for multi-messenger astrophysics. A little considered source of electromagnetic transients accompanying compact binary systems is a neutron star ocean, the external fluid layer encasing a neutron star. We present a groundwork study into tidal waves in neutron star oceans and their consequences. Specifically, we investigate how oscillation modes in neutron star oceans can be tidally excited during compact binary inspirals and parabolic encounters to produce tidal waves. We find that neutron star oceans can sustain tidal waves with frequencies under 100 mHz. Our results suggest that resonant neutron star ocean tidal waves may serve as a never-before studied source for precursor electromagnetic emission prior to neutron star-black hole and binary neutron star mergers. Resonant neutron star ocean tidal waves, whose energy budget can reach 10^{45} erg, may serve as very early warning signs ($\sim 1 - 10$ yr before merger) for compact binary mergers if accompanied by electromagnetic flares. Similarly, excited ocean tidal waves will coincide with neutron star parabolic encounters. Depending on the neutron star ocean model and a flare emission scenario, flares may be detectable by Fermi and NuSTAR out to ~ 100 Mpc with detection rates as high as ~ 7 yr⁻¹ for binary neutron stars and ~ 0.6 yr⁻¹ for neutron star-black hole binaries. Observations of emission from neutron star ocean tidal waves along with gravitational waves will provide insight into the equation of state at the neutron star surface, the composition of neutron star oceans and crusts, and neutron star geophysics.

Key words: (transients:) black hole - neutron star mergers – (transients:) neutron star mergers – stars: oscillations – gravitational waves – X-rays: bursts

1 INTRODUCTION

With the recent detections of gravitational waves (GWs) from compact binary systems by GW detectors such as LIGO, Virgo, and KAGRA (Acernese et al. 2015; LIGO Scientific Collaboration 2015; LIGO Scientific Collaboration & Virgo Collaboration 2017; Akutsu et al. 2019; The LIGO Scientific Collaboration & the Virgo Collaboration 2021; LIGO Scientific Collaboration et al. 2021), neutron stars have become a prime topic of astrophysics research. Neutron stars represent a unique class of stellar objects in that, though very dense, these objects emit light, making them a candidate for combined GW-Electromagnetic multi-messenger astrophysical searches (Rosswog 2015; Abbott et al. 2018). Neutron stars are thought to consist of three distinct layers: a very dense fluid core, a solid crust, and an external fluid ocean (Lattimer & Prakash 2001). The respective properties of each of these neutron star layers are largely

dependent on the neutron star equation of state (Lattimer & Prakash 2001), whose details remain an active problem in nuclear physics and astrophysics. Neutron star structure may be probed through detections of X-ray bursts (Bildsten & Cutler 1995; Strohmayer & Mahmoodifar 2014; Chambers & Watts 2020), gamma ray bursts, (Tsang et al. 2012; Tsang 2013; Suvorov & Kokkotas 2020), ejecta from compact binary inspirals (Metzger et al. 2010; Metzger & Fernández 2014; Geroyannis et al. 2017; Metzger 2017; Radice et al. 2018; Metzger 2019; Soares-Santos et al. 2017; Cowperthwaite et al. 2017; Nicholl et al. 2017; Chornock et al. 2017; Bartos & Marka 2019), and GWs (Andersson & Kokkotas 1998; Ferrari 2010; Suvorov 2018; Chatziioannou 2020).

In recent years, GW astrophysics has become a unique observational tool to study neutron star physics. A number of open questions have been posed about the properties of neutron stars whose answers may lie in the rich capabilities of present and future GW detectors and multi-messenger astrophysics. Works have investigated the possibility of mountains formed on the surfaces of spinning

* E-mail: ags2198@columbia.edu

neutron stars whose asymmetries could generate detectable continuous GWs (Ushomirsky et al. 2000; Osborne & Jones 2020; Gittins et al. 2021; Gittins & Andersson 2021). Searches for continuous GW sources potentially originating from these spinning neutron stars have been undertaken (Aasi et al. 2015; Papa et al. 2020; The LIGO Scientific Collaboration et al. 2021c; Abbott et al. 2022; The LIGO Scientific Collaboration et al. 2022). From continuous GW searches, geophysical structure and seismology of neutron stars may be further probed (Geroyannis et al. 2017; Yang et al. 2018; Suvorov 2018; Andersson 2021).

Neutron stars exhibit a variety of pulsational modes (McDermott et al. 1988; Reisenegger & Goldreich 1994; Lai 1994; Passamonti et al. 2006; Samuelsson et al. 2007; Passamonti & Andersson 2012). Neutron star oscillation modes are associated with the restoring forces and structure of the star. These modes include fundamental modes or f -modes (Lau et al. 2010; LIGO Scientific Collaboration & Virgo Collaboration 2017; Wen et al. 2019; LIGO Scientific Collaboration et al. 2021), pressure modes or p -modes (Bandari 2014), gravity modes or g -modes (McDermott et al. 1988; Bildsten & Cutler 1995; Bildsten et al. 1996; Deibel 2016; Andersson & Pnigouras 2020; Passamonti et al. 2021; Kuan et al. 2021b), r -modes in rotating neutron stars (Haskell 2015; Mitidis 2015; Ma et al. 2021; Chambers & Watts 2020), and interface modes or i -modes (McDermott et al. 1988; Passamonti & Andersson 2012). These modes may be excited during accretion (Reisenegger & Goldreich 1994; Deibel 2016) or by tides (Lai 1994; Ho & Lai 1999; Gittins et al. 2021).

Oscillations in neutron stars have been studied in connection with emission of electromagnetic radiation. Oscillations in neutron star oceans induced by accretion have been considered in many previous works (Bildsten & Cutler 1995; Bildsten et al. 1996; Heyl 2004; Deibel 2016; Chambers & Watts 2020; van Baal et al. 2020). Thermonuclear burning on the surfaces of neutron stars during accretion can excite oscillation modes, which could be associated with oscillations in type-I X-ray bursts (Hansen & van Horn 1975; Woosley & Taam 1976; Maraschi & Cavaliere 1977; Bildsten & Cutler 1995; Spitkovsky et al. 2002; Lee 2004; Piro & Bildsten 2005; Chambers et al. 2018; Chambers & Watts 2020). Observed thermonuclear X-ray bursts on neutron stars potentially show signs of ocean mode oscillation (Galloway et al. 2008; Bilous & Watts 2019; Roy et al. 2021; Bult et al. 2021).

Because neutron stars have been observed to exist in binaries, tidal deformations play a role in neutron star physics as well. A neutron star's response to a tidal force is largely dependent on its internal properties, including its oscillation modes (Lai 1994). Observations of tidally excited oscillation modes could shed light on the composition of neutron stars.

In this work, we analyze neutron star ocean oscillations generated by dynamical tidal processes during interactions with other compact objects. We principally consider ocean tidal waves in compact binary inspirals where the tidal forces become resonant with neutron star oceans. We also investigate tidal waves from unbound neutron star encounters. We present models for neutron star oceans and investigate the amplitudes of tidal waves sustainable in these neutron star oceans. Ultimately, we consider emission that tidally excited neutron star oceans might produce, including electromagnetic flares and GW emission. All of our analysis is performed using Newtonian theory due to the exploratory and phenomenological nature of this study.

We divide the paper into the following sections. In section 2, we present the background neutron star and equation of state models used, as well as introduce the three neutron star ocean models

investigated. In section 3, we discuss the equations of motion for neutron star oscillations and determine the neutron star ocean oscillation modes for our ocean models. In section 4, we discuss the tidal interaction that drives ocean waves and compute tidal wave properties for each of the oceans and orbital configurations considered. In section 5, we discuss our results and their consequences, including potential emission produced by neutron star ocean tidal waves. In section 6, we conclude.

2 BACKGROUND NEUTRON STAR AND OCEAN MODEL

We first provide our neutron star model. In order to focus on the properties of the neutron star ocean, we use a simple model of a rigid solid sphere surrounded by a fluid ocean whose depth we vary.

To solve for the background density ρ and pressure p of the neutron star, we use the classical equilibrium equations for a spherically symmetric fluid

$$\frac{dp}{dr} = -\rho g, \quad (1a)$$

$$\frac{dM}{dr} = 4\pi G r^2 \rho, \quad (1b)$$

where $M(r)$ is the mass enclosed at a given radius, G is Newton's gravitational constant, and $g = \frac{GM(r)}{r^2}$ is the magnitude of gravitational acceleration (Chandrasekhar 1957). Given an equation of state, these equations can be solved and the star's background pressure and density can be obtained. In this work, we use a polytropic equation of state (Ferrari et al. 2010)

$$p = K \rho^\Gamma, \quad (2)$$

where K is a proportionality constant. Choosing $\Gamma = 2$ yields the analytic solution for the mass density when $r < R_{NS}$

$$\rho(r) = \rho_c \frac{\sin \sqrt{\frac{4\pi G}{2K}} r}{\sqrt{\frac{4\pi G}{2K}} r}, \quad (3)$$

where ρ_c is the density at the center of the star and R_{NS} is the radius of the neutron star (Chandrasekhar 1957). When $r > R_{NS}$, we have $\rho(r) = 0$. Note that the radius of the star is completely specified by the constant K . We estimate K by assuming

$$R_{NS} \approx \frac{p_c}{|\frac{dp}{dr}|} = \frac{K \rho_c^\Gamma}{\rho_c g} \approx \frac{K \rho_c^\Gamma}{G \rho_c^2 R_{NS}}, \quad (4)$$

where the subscript c denotes the quantity evaluated at the core. If $\Gamma = 2$, we arrive at $K \approx GR_{NS}^2$. For this study, we assume our neutron star is non-rotating and has no magnetic field. The inclusion of rotation and magnetization, if small enough, will serve as a perturbation to the oscillation mode structure and frequency without changing the physics (Kuan et al. 2021c,d; Krüger et al. 2021). Because we are interested in early inspirals, the effects of general relativity should not play a role in spinning up the rotation of neutron stars. Additionally, while we expect effects such as tidal locking to spin up neutron stars, we do not consider them in our study. We leave consideration of rotating and magnetized neutron stars to future work.

2.1 Neutron Star Ocean Depth

The depth of the neutron star ocean is dependent on the density at which the neutron star crust melts. The top of the crust is typically considered to be a body-centered cubic (bcc) Coulomb crystal (Bildsten & Cutler 1995; Haensel et al. 2007; Horowitz & Kadau 2009; Baiko & Chugunov 2018; Gittins et al. 2020). In a Coulomb crystal, the ions which compose the lattice interact exclusively by the Coulomb interaction (Chambers et al. 2018) because the electron screening in the outer crust is weak (Chamel & Haensel 2008). The Coulomb crystal undergoes a phase transition when the thermal energy exceeds the electric binding energy of the material by some critical factor γ (Farouki & Hamaguchi 1993). The crust melts when the following condition is met:

$$k_B T \geq \frac{1}{\gamma} \frac{1}{4\pi\epsilon_0} \frac{Z^2 e^2}{d}, \quad (5)$$

where k_B is Boltzmann's constant, T is the temperature, ϵ_0 is the permittivity of free space, Z is the proton number of atomic nuclei in the lattice, e is electron charge, and d is the mean spacing between nuclei. Molecular dynamics studies have found $\gamma \approx 173$ (Farouki & Hamaguchi 1993). Assuming that the number density of atomic

nuclei is $n_N = (\frac{4}{3}\pi d^3)^{-1}$, the mass density ρ_o at which the crust melts and the ocean forms is

$$\begin{aligned} \rho_o &= A m_n n_N = \frac{3}{4\pi} A m_n \left(\gamma \frac{4\pi\epsilon_0 k_B T}{Z^2 e^2} \right)^3 \\ &\approx 2.705 \times 10^{10} \text{ g cm}^{-3} \left(\frac{A}{16} \right) \left(\frac{8}{Z} \right)^6 \left(\frac{T}{10^8 \text{ K}} \right)^3, \end{aligned} \quad (6)$$

where A is the atomic mass of the nuclei in the lattice, m_n is nucleon mass, and we have used the condition in equation 5 for d at the transition between the neutron star crust and ocean. Equation 6 shows the melting density's strong dependence on atomic number of the ions and temperature. More proton-rich nuclei will reduce the density at which the ocean begins.

By plugging equation 6 into the left-hand side of equation 3, we determine the radius at which the ocean begins and by extension the depth of the ocean as a function of A , Z , and T . Since neutron star oceans are very shallow compared to the size of the neutron star (Bildsten & Cutler 1995; Bildsten et al. 1996; Urpin 2004; Deibel 2016; van Baal et al. 2020), we approximate r in the denominator of equation 3 as the stellar radius R_{NS} . The radius at which the neutron star ocean begins for a $\Gamma = 2$ polytropic equation of state is

$$r_o = \sqrt{\frac{2K}{4\pi G}} \left[\arccos \left(\sqrt{\frac{4\pi G}{2K}} R_{NS} \frac{3}{4\pi} \frac{A m_n}{\rho_c} \left(\gamma \frac{4\pi\epsilon_0 k_B T}{Z^2 e^2} \right)^3 \right) + \frac{\pi}{2} \right]. \quad (7)$$

In this work, we consider crusts primarily made up of three elements thought to be found in neutron star crusts and oceans due to their production by r-processes (Meisel et al. 2018): carbon with $Z = 6$ and $A = 12$, oxygen with $Z = 8$ and $A = 16$, and iron with $Z = 26$ and $A = 56$. For referential convenience throughout the rest of this paper, we will refer to the three different oceans as being carbon, oxygen, or iron oceans. Neutron star crust temperatures are typically $T \sim 10^7$ K when the crust is in thermal equilibrium with the core (Brown et al. 1998; Brown & Cumming 2009). The temperature of the neutron star ocean floor can reach $T \sim 10^8$ K during accretion (Fujimoto et al. 1984; Haensel & Zdunik 1990, 2003, 2008). Accreting neutron stars with crust temperatures of $T \sim 10^8$ K have oceans whose temperatures decrease to 10^6 K at the surface (Miralda-Escude et al. 1990; Chamel & Haensel 2008). In our study, we neglect the effect of the temperature gradient across the ocean. We will discuss our choice for crust temperature in section 3.4.1.

3 NEUTRON STAR OCEAN OSCILLATION MODES

In order to study the waves in neutron star oceans, we solve for the dynamical response of neutron star matter. To do this, we use the formalism of Lagrangian perturbation theory for fluids (Friedman & Schutz 1978). We use the Newtonian formalism typically used for solving the oscillation modes of neutron stars (Dziembowski 1971; Ledoux 1974; McDermott et al. 1988; Passamonti & Andersson 2012), as it allows us to study the dynamical response to tidal forces (Lai 1994; Reisenegger & Goldreich 1994; Tsang et al. 2012; Tsang 2013; Passamonti et al. 2021).

3.1 Equations of Motion

The classical equation of motion for Lagrangian perturbative displacements of a fluid in hydrostatic equilibrium is

$$\partial_t^2 \vec{\xi} + \frac{\nabla \delta p}{\rho} - \frac{\delta \rho}{\rho^2} \nabla p + \nabla \delta \phi = -\nabla \chi, \quad (8)$$

where $\vec{\xi}$ is the Lagrangian displacement vector, ρ is the background density of the fluid, p is the background pressure of the fluid, $\delta \rho$ is the Eulerian perturbation of the density, δp is the Eulerian perturbation of the pressure, $\delta \phi$ is the Eulerian perturbation of the gravitational potential, and χ is an unspecified (for now) external potential that drives the system.

The Lagrangian perturbation for density can be written as

$$\Delta \rho = \delta \rho + \vec{\xi} \cdot \nabla \rho = -\rho \nabla \cdot \vec{\xi}, \quad (9)$$

where the first equality is the definition of the Lagrangian perturbation in terms of the Eulerian perturbation and the second equality arises from conservation of mass (Friedman & Schutz 1978). If the oscillations are adiabatic, the Lagrangian perturbations for pressure and density are related to one another by

$$\frac{\Delta p}{\rho} = \frac{1}{\Gamma_1} \frac{\Delta \rho}{\rho}, \quad (10)$$

where Γ_1 is the adiabatic index. We note that Γ_1 does not necessarily equal Γ . When $\Gamma_1 \neq \Gamma$, the neutron star is stratified and can sustain internal g -modes (McDermott et al. 1988; Bildsten & Cutler 1995; Bildsten et al. 1996; Andersson & Pnigouras 2020; Passamonti et al. 2021).

The final equation of motion that governs this system is the perturbative form of the Poisson equation

$$\nabla^2 \delta \phi = 4\pi G \delta \rho. \quad (11)$$

Since the ocean is the uppermost layer of the star and typically very shallow, the perturbation of the gravitational potential $\delta\phi$ and its gradient $\nabla\delta\phi$ must be very small compared to the background gravitational potential ϕ and the background gravitational acceleration g . As such, we employ the Cowling approximation (Cowling 1941), which approximates $\delta\phi \approx 0$ and $\nabla\delta\phi \approx 0$. Consequently, we neglect the appearance of $\delta\phi$ in equation 8.

In this section, we set $\chi = 0$ and study the homogeneous solutions to equation 8. First, we define a perturbation to the chemical potential per nucleon mass $\delta\tilde{\mu}$ which is related to the perturbation of pressure by

$$\delta p = n_N \delta\mu = \rho\delta\tilde{\mu}, \quad (12)$$

where $\delta\mu$ is the normal chemical potential. Inserting equation 12 for δp into equation 8 and applying the Cowling approximation gives

$$\partial_t^2 \vec{\xi} + \nabla\delta\tilde{\mu} = 0. \quad (13)$$

We use equations 9 and 10 to obtain the other equation we need to solve this system. From the definition of the Lagrangian perturbation (Friedman & Schutz 1978), we have

$$\Delta p = \delta p + \vec{\xi} \cdot \nabla p = \rho\delta\tilde{\mu} + \xi_r \frac{dp}{dr}, \quad (14)$$

where ξ_r is the radial component of $\vec{\xi}$ and the second equality comes from equation 12 and spherical symmetry (i.e. $\nabla p = \frac{dp}{dr}$). Substituting equations 14 and 9 into equation 10, we obtain

$$\nabla \cdot \vec{\xi} = -\frac{1}{\Gamma_1 p} \left(\rho\delta\tilde{\mu} + \xi_r \frac{dp}{dr} \right). \quad (15)$$

Equations 13 and 15 are a system of partial differential equations which can be solved using a clever ansatz for $\vec{\xi}$. We ansatz that $\vec{\xi}$ can be decomposed into normal modes such that (Dziembowski 1971; Ledoux 1974; McDermott et al. 1988; Passamonti & Andersson 2012)

$$\vec{\xi} = \sum_n e^{i\omega_n t} \vec{\xi}_n, \quad (16)$$

where ω_n is the angular frequency of a resonant mode and $\vec{\xi}_n$ is the eigenfunction that solves the equation

$$(\mathcal{L} - \rho\omega^2)\vec{\xi} = 0, \quad (17)$$

where \mathcal{L} is an operator defined such that $\mathcal{L}\vec{\xi} = \rho\nabla\delta\tilde{\mu}$ (Press & Teukolsky 1977; Passamonti et al. 2021). The index n denotes the mode. The orthogonality of these modes requires (Press & Teukolsky 1977; Lai 1994; Passamonti et al. 2021)

$$\langle \vec{\xi}_n | \vec{\xi}_m \rangle = \int \rho \vec{\xi}_n^* \cdot \vec{\xi}_m dV = A_n^2 \delta_{nm}, \quad (18)$$

where the integral is over the volume of the star, $\vec{\xi}_n^*$ is the complex conjugate of $\vec{\xi}_n$, A_n^2 is the normalization factor, and δ_{mn} is the Kronecker delta. We ansatz a form for $\vec{\xi}_n$ as (Dziembowski 1971; Ledoux 1974; McDermott et al. 1988; Passamonti & Andersson 2012)

$$\vec{\xi}_n = \left(U(r)Y_{lm}(\theta, \phi), V(r)\partial_\theta Y_{lm}(\theta, \phi), \frac{V(r)}{\sin\theta}\partial_\phi Y_{lm}(\theta, \phi) \right), \quad (19)$$

where $Y_{lm}(\theta, \phi)$ are the spherical harmonic functions (Jackson 1962), ∂_x is the partial derivative with respect to the variable x , and $U(r)$ and $V(r)$ are functions of the radial coordinate that must be solved for. We also assume that $\delta\tilde{\mu}$ can be written as

$\delta\tilde{\mu} = \delta\tilde{\mu}(r)Y_{lm}(\theta, \phi)e^{i\omega t}$. Plugging our ansatz for $\vec{\xi}$ and $\delta\tilde{\mu}$ into equations 13 and 15 and cancelling out common factors gives

$$-\omega^2 U + \frac{d}{dr}\delta\tilde{\mu} = 0, \quad (20a)$$

$$-\omega^2 V + \frac{\delta\tilde{\mu}}{r} = 0, \quad (20b)$$

$$\frac{dU}{dr} + \frac{2}{r}U - \frac{l(l+1)}{r}V = -\frac{1}{\Gamma_1 p} \left(\rho\delta\tilde{\mu} + U\frac{dp}{dr} \right). \quad (20c)$$

Rearranging equations 20a and 20c and using the relationship in equation 20b, this system reduces to two ordinary differential equations

$$\frac{d}{dr}\delta\tilde{\mu} = \omega^2 U, \quad (21a)$$

$$\frac{dU}{dr} = -\left(\frac{2}{r} + \frac{1}{\Gamma_1 p} \frac{dp}{dr} \right) U + \left(-\frac{\rho}{\Gamma_1 p} + \frac{l(l+1)}{r^2\omega^2} \right) \delta\tilde{\mu}. \quad (21b)$$

We write these equations in terms of the dimensionless variables $y_1 = \frac{U}{r}$ and $y_2 = \frac{\delta\tilde{\mu}}{rg}$, where g is the background gravitational field as a function of radius. We obtain

$$\frac{dy_1}{dr} = -\left(\frac{3}{r} + \frac{1}{\Gamma_1 p} \frac{dp}{dr} \right) y_1 + \left(-\frac{\rho}{\Gamma_1 p} + \frac{l(l+1)}{r^2\omega^2} \right) g y_2, \quad (22a)$$

$$\frac{dy_2}{dr} = \frac{\omega^2}{g} y_1 - \left(\frac{1}{r} + \frac{1}{g} \frac{dg}{dr} \right) y_2. \quad (22b)$$

In the single fluid limit and the Cowling approximation, the equations in section A1 of Passamonti & Andersson (2012) reduce to equations 22. Given boundary conditions at the ocean floor and surface, a value for Γ_1 (which is not constant in general), and a value of l , we may solve these equations as a boundary value problem. Solutions will give us the natural oscillation modes for the l th harmonic.

3.2 Boundary Conditions

Since the mode frequency ω is unknown, we must apply three boundary conditions to solve equations 22. For our simple neutron star model, we assume the crust is stiff and cannot sustain oscillations. At the ocean floor we apply the condition

$$y_1(r_o) = 0. \quad (23)$$

This is the same condition applied by Bildsten & Cutler (1995) to solve for deep ocean g -modes. Though we use an unstratified neutron star model for simplicity and do not find g -modes, we assume the ocean modes do not penetrate below the ocean due to the rigidity of neutron star crusts (Horowitz & Kadau 2009). At the surface of the ocean we apply the condition $\Delta p = 0$ (McDermott et al. 1988; Lai 1994). In our variables, this becomes

$$0 = y_1(R_{NS}) - y_2(R_{NS}). \quad (24)$$

Additionally, so that we can find the functional form of the oscillation modes, we apply a normalization condition at the surface of the ocean,

$$y_1(R_{NS}) = 1. \quad (25)$$

With these three boundary conditions, our system is closed and solvable.

3.3 Semi-Analytic Ocean Modes and Tidal Resonance

We now provide a simple analytic argument for how the ocean mode frequency scales with model parameters. This will also give the time of tidal resonance as a function of model parameters. We assume that the ocean mode frequency ω is functionally related to the inverse of the sound crossing time inside the ocean

$$\omega \sim \frac{1}{R_{NS}} \sqrt{\frac{p_o}{\rho_o}}, \quad (26)$$

where p_o is the pressure at the bottom of the ocean. Supplying a general polytropic equation of state gives

$$\omega \sim \frac{1}{R_{NS}} \sqrt{K \rho_o^{\Gamma-1}}. \quad (27)$$

We now substitute in the expression for ρ_o from equation 6 to obtain

$$\omega \sim \frac{K^{\frac{1}{2}}}{R_{NS}} \left(\gamma \left(\frac{3}{4\pi} m_n \right)^{\frac{1}{3}} \frac{4\pi\epsilon_0 k_B}{e^2} \right)^{\frac{3\Gamma-3}{2}} A^{\frac{\Gamma-1}{2}} Z^{3-3\Gamma} T^{\frac{3\Gamma-3}{2}}. \quad (28)$$

One can see that the mode frequency increases as a function of T and A and decreases as a function of Z for $\Gamma > 1$.

Since we are interested in tidal resonances during compact

binary inspirals, we can estimate the time before compact binary merger of an ocean tidal resonance. Tidal resonances should occur when

$$\dot{\Phi} = \frac{\omega}{m}, \quad (29)$$

where $\dot{\Phi}$ is the orbital frequency of the compact binary and m is the spherical harmonic index. For circular binaries, we have

$$\dot{\Phi} = \sqrt{\frac{G(M+M_*)}{D^3}}, \quad (30)$$

where M_* is the mass of the companion object and D is orbital separation. The time to merger for a given orbital separation D is (Peters 1964)

$$t_m = \frac{D^4}{4\beta}, \quad (31)$$

where β is

$$\beta = \frac{64}{5} \frac{G^3 M M_* (M+M_*)}{c^5}, \quad (32)$$

where c is the speed of light. Combining equations 28, 29, 30, and 31 gives an expression for the time of resonance as

$$t_r \sim \frac{1}{4\beta} \left(\frac{R_{NS}^2 m^2 G (M+M_*)}{K} \right)^{\frac{4}{3}} \left(\gamma \left(\frac{3}{4\pi} m_n \right)^{\frac{1}{3}} \frac{4\pi\epsilon_0 k_B}{e^2} \right)^{4-4\Gamma} A^{\frac{4-4\Gamma}{3}} Z^{8\Gamma-8} T^{4-4\Gamma}. \quad (33)$$

These very rough analytical estimates for the mode frequency and resonance time allow us to limit the scope of our study to physically interesting neutron star ocean scenarios.

3.4 Ocean Mode Results

We now discuss the numerical values we choose for neutron star parameters and present the neutron star ocean mode results.

3.4.1 Neutron Star Model Parameters

We assign the parameters of our neutron star for our computation. We choose $\Gamma = 2$ as was done by Passamonti et al. (2021). Since $R \sim 10$ km for neutron stars, the value of K that we use is $K = 6.67 \times 10^4 \text{ cm}^5 \text{ g}^{-1} \text{ s}^{-2}$ from $K \approx GR_{NS}^2$. Our neutron star model has a central density $\rho_c = 10^{15} \text{ g cm}^{-3}$. These choices yield a neutron star that has radius $R_{NS} = 12.5$ km and a mass $M = 1.25 M_\odot$. This is just smaller than the peak mass of $1.39 M_\odot$ for the galactic neutron star population (Antoniadis et al. 2016; Alsing et al. 2018).

For our computations, we fix the temperature $T = 10^8$ K at the crust-ocean interface, as this gives resonance times, which we will discuss in more detail in section 4.2.1, on the order of ~ 10 yr for a binary neutron star (BNS). Cold neutron stars ($T \sim 10^7$ K in the crust) will have less dense and by extension lower pressure oceans, making the ocean modes very low frequency and the tidal resonances occur much earlier. From equation 33, we see that $t_r \propto T^2$ when $\Gamma = 2$. As a consequence, colder oceans will have resonance times > 100 yr before merger, which is practically too long for the coincident detection of tidal resonances with compact

binary mergers. To get temperatures as hot as $T = 10^8$ K in the crust, one typically needs heating due to accretion (Fujimoto et al. 1984; Haensel & Zdunik 1990, 2003, 2008). For this simple study, we do not account for accretion when computing the tidal wave amplitudes or energies.

The ratio of the ocean floor depth to the neutron star radius is independent of the choice of K in the equation of state. From equation 7, we find that the ocean floor depths of the three oceans are $D_c = 1.14 \times 10^{-4} R_{NS}$, $D_o = 2.71 \times 10^{-5} R_{NS}$, and $D_i = 8.03 \times 10^{-8} R_{NS}$ for carbon, oxygen, and iron, respectively.

The carbon and oxygen neutron star oceans form below the electron capture density of those elements, so the bottoms of these oceans would be a dense plasma of ions and electrons (Bildsten & Cutler 1995). For simplicity, we neglect the effect of the ocean having distinct layers and leave this to future work.

3.4.2 Neutron Star Ocean Modes

We solve equations 22 using a four-stage Runge-Kutta scheme. We use a shooting method (Press et al. 1986) to obtain the frequencies of each mode. Because tidal forces correspond to $l \geq 2$ spherical harmonics, $l = 0$ and $l = 1$ modes will remain practically unaffected by tidal forces, so we do not solve for them. We solve for only $l = 2$ modes as those are the modes most likely to be excited tidally. As noted previously, we assume the neutron star is unstratified so that it cannot sustain internal g -modes and $\Gamma_1 = \Gamma = 2$. As such, our ocean will only have f - and p -modes. For each ocean model, we find that the ocean can sustain one $l = 2$ mode with a frequency below the

orbital frequency at which two neutron stars merge ($\gtrsim 10^3$ Hz) (Abbott et al. 2019).

Each of the mode frequencies we find is below 100 mHz. We note that stratified models can produce g -modes with frequencies of order ~ 1 Hz (Bildsten & Cutler 1995). Table 1 shows the densities at the ocean floor, the depths, and the mode frequencies of neutron star oceans with crusts primarily composed of these three elements at a temperature of $T = 10^8$ K, as well as integrals computed later in the paper. The frequency of the mode increases with the density at which the ocean forms. Carbon oceans have the highest mode frequency at 85.4 mHz, while less dense iron oceans have a mode frequency of 59.7 mHz. We note that the fully computed mode frequencies are each about an order of magnitude lower than the rough estimates obtained from equation 28.

Figure 1 plots the radial and tangential components of the Lagrangian displacement for the three ocean modes. Each mode exhibits similar structure. The radial component $U(r)$ for each ocean has no nodes and peaks near the middle of the ocean. The tangential component $V(r)$ varies little throughout the three oceans, but well exceeds the radial component throughout the ocean due to the strength of gravity in the ocean.

4 TIDAL INTERACTION

We now add the potential χ back to equation 8 and solve, making χ is the tidal potential from a nearby companion object. Assuming the companion object is a point mass and it orbits in the plane of the equator of the neutron star, the tidal potential takes the form (Press & Teukolsky 1977; Lai 1994)

$$\chi = - \sum_{l=2}^{\infty} \sum_{m=-l}^l \frac{GM_* r^l}{D(t)^{l+1}} W_{lm} e^{-im\Phi(t)} Y_{lm}(\theta, \phi), \quad (34)$$

where M_* is the mass of the companion, $D(t)$ is the separation of the two stars as a function of time, $\Phi(t)$ is the true anomaly, and W_{lm} is the numerical coefficient (Press & Teukolsky 1977)

$$W_{lm} = (-1)^{\frac{l+m}{2}} \frac{(\frac{4\pi}{2l+1}) (l-m)! (l+m)!^{\frac{1}{2}}}{2^l (\frac{l-m}{2})! (\frac{l+m}{2})!}, \quad (35)$$

where $l+m$ must be even.

Adding the external potential χ to equation 13, we have

$$\partial_t^2 \vec{\xi} + \nabla \delta \tilde{\mu} = -\nabla \chi. \quad (36)$$

Since we have obtained normal mode solutions to the homogenous equation $\vec{\xi}_n$, we may ansatz a solution to equation 36 (Lai 1994)

$$\vec{\xi} = \sum_n a_n(t) \vec{\xi}_n, \quad (37)$$

where $a(t)$ is an amplitude that scales the eigenfunction and encodes all time dependence of $\vec{\xi}$. Using the operator $\mathcal{L}\vec{\xi} = \rho \nabla \delta \tilde{\mu}$ defined in Section 3.1, equation 36 becomes

$$(\rho \partial_t^2 + \mathcal{L}) \vec{\xi} = -\rho \nabla \chi. \quad (38)$$

Substituting in our ansatz for $\vec{\xi}$ gives

$$-\rho \nabla \chi = \sum_n \rho \ddot{a}_n(t) \vec{\xi}_n + a_n(t) \mathcal{L} \vec{\xi}_n = \sum_n (\ddot{a}_n(t) + \omega_n^2 a_n(t)) \rho \vec{\xi}_n, \quad (39)$$

where the last equality arises from equation 17. We may use the

orthogonality condition in equation 18 to isolate an equation for $a_n(t)$. Applying orthogonality yields

$$\ddot{a}_n(t) + \omega_n^2 a_n(t) = -\frac{1}{A_n^2} \int \rho \vec{\xi}_n^* \cdot \nabla \chi dV. \quad (40)$$

Plugging in the tidal potential from equation 34, equation 40 becomes

$$\ddot{a}_n(t) + \omega_n^2 a_n(t) = \frac{GM_*}{D(t)^{l+1}} W_{lm} \frac{Q_n}{A_n^2} e^{-im\Phi(t)}, \quad (41)$$

where Q_n is the overlap integral defined by (Press & Teukolsky 1977; Lai 1994; Tsang et al. 2012; Tsang 2013; Andersson & Pnigouras 2020; Passamonti et al. 2021)

$$Q_n = \int \rho \vec{\xi}_n^* \cdot \nabla (r^l Y_{lm}(\theta, \phi)) dV = l \int \rho (U + V(l+1)) r^{l+1} dr, \quad (42)$$

where we have used equation 19 to obtain the last equality. Note that the overlap integral is entirely a property of the mode and quantifies how strongly the mode gets excited by tidal forces. We define a normalized overlap integral, dimensionless for the $l=2$ modes, as

$$\tilde{Q}_n = \frac{Q_n}{A_n^2}. \quad (43)$$

In table 1, we report the normalized overlap integrals for each of the three ocean modes. Note that these overlap integrals are much smaller than the overlap integrals reported by Passamonti et al. (2021) for neutron star modes that penetrate throughout the whole star because of how small the ocean is.

Following the analysis of Lai (1994), we perform a change of variables to solve equation 41 where

$$a(t) = GM_* \tilde{Q}_n W_{lm} b(t) e^{-im\Phi(t)} \quad (44)$$

and $b(t)$ is the new function to solve for. In terms of $b(t)$, equation 41 becomes

$$\ddot{b} - 2im\dot{\Phi}\dot{b} + (\omega^2 - m^2\dot{\Phi}^2 - im\ddot{\Phi})b = \frac{1}{D(t)^{l+1}}. \quad (45)$$

If we decompose b into a real part b^r and an imaginary part b^i , equation 45 becomes the following two equations:

$$\ddot{b}^r + 2m\dot{\Phi}\dot{b}^i + m\ddot{\Phi}b^i + (\omega^2 - m^2\dot{\Phi}^2)b^r = \frac{1}{D(t)^{l+1}}, \quad (46a)$$

$$\ddot{b}^i - 2m\dot{\Phi}\dot{b}^r - m\ddot{\Phi}b^r + (\omega^2 - m^2\dot{\Phi}^2)b^i = 0. \quad (46b)$$

Given an orbital trajectory for a companion celestial body, equations 46a and 46b can be solved. By plugging solutions to equations 46a and 46b back into equation 44, the tidal wave amplitude $a(t)$ in the neutron star ocean can be found.

4.1 Tidal Interaction Scenarios

We consider three tidal interaction scenarios: a BNS inspiral in a circular orbit, a neutron star-black hole binary inspiral (NSBH) in a circular orbit, and an unbound parabolic encounter between two neutron stars (NSPE). While NSPEs are expected to be fairly rare (Tsang 2013) due to the low presence of neutron stars predicted in stellar clusters (Bae et al. 2014; Belczynski et al. 2018; Ye et al. 2020; Mandel & Broekgaarden 2022), tidal interactions from these events remain relatively unexplored beyond Tsang (2013), so we consider them in this work. In the following subsections, we enumerate the initial conditions and orbital parameters in each of these scenarios.

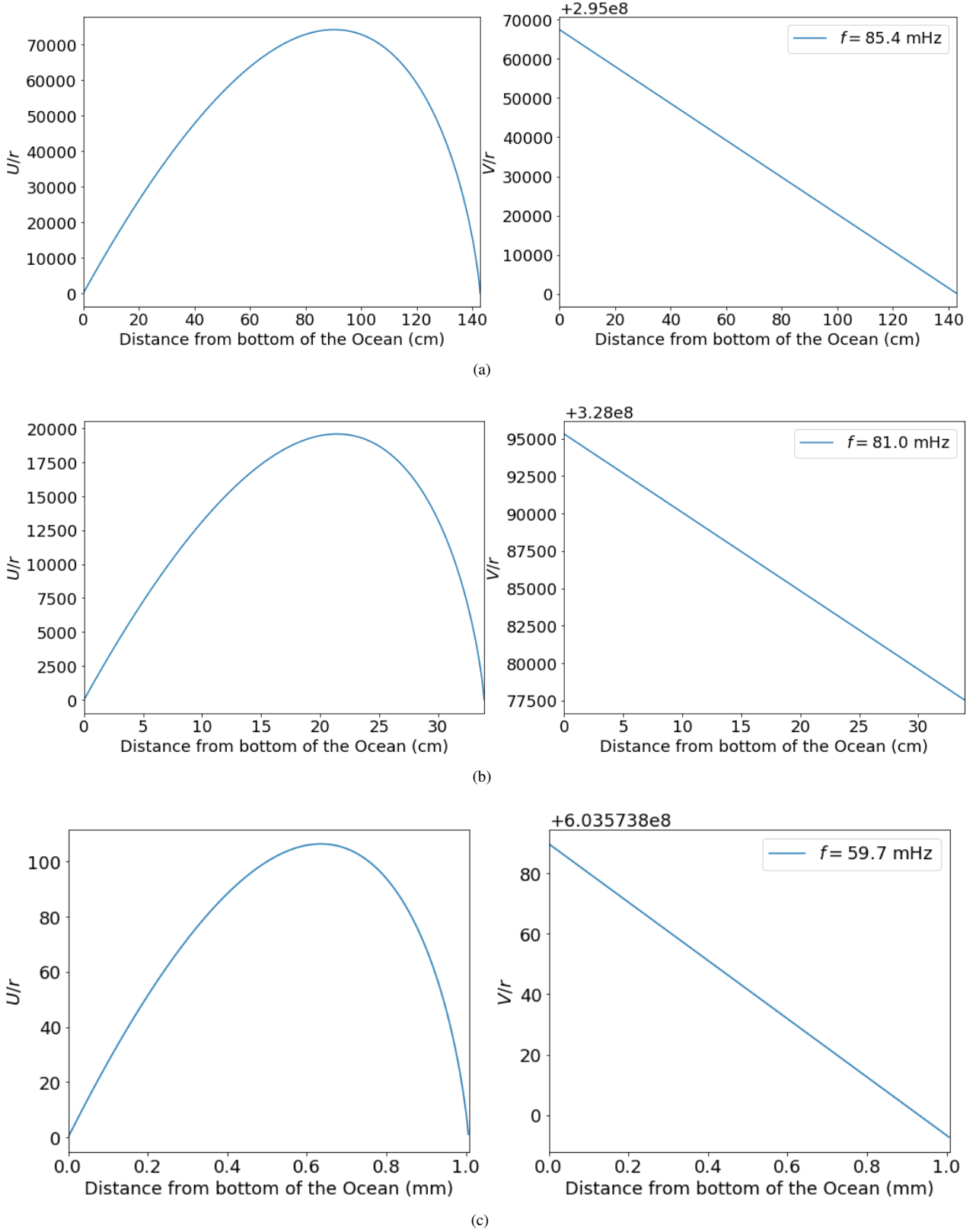


Figure 1. The fundamental mode for the three neutron star ocean models we study in this paper: a) the carbon ocean, b) the oxygen ocean, and c) the iron ocean. The left-hand plots show the dimensionless function $\frac{U(r)}{r}$ as a function of distance from the ocean floor while the right hand plots show the dimensionless function $\frac{V(r)}{r}$ as a function of distance from the ocean floor. The mode frequency of each ocean model is shown in the legend of the right hand plot.

Ocean Makeup	Carbon	Oxygen	Iron
Z	6	8	26
A	12	16	56
Melting Density at $T = 10^8$ K (g cm^{-3})	1.10×10^{11}	2.71×10^{10}	8.03×10^7
Ocean depth (R_{NS})	1.14×10^{-4}	2.71×10^{-5}	8.03×10^{-8}
Ocean depth when $R_{NS} = 12.5$ km (cm)	143	33.9	1.01×10^{-1}
Angular Mode frequency ω (s^{-1})	0.53654584	0.50877963	0.375104944
Mode frequency f (mHz)	85.39	80.97	59.70
\tilde{Q}_n	3.3894×10^{-9}	3.0479×10^{-9}	1.6568×10^{-9}
H_n (g cm^2)	3.524×10^{41}	8.365×10^{40}	2.482×10^{38}

Table 1. The properties of the three neutron star ocean materials we consider in this work. We show the atomic number and mass of each element that we consider as the dominant substance in a $T = 10^8$ K neutron star crust as well as the densities at the ocean floors calculated from equation 6, the ocean depths from equation 7, the angular mode frequencies and mode frequencies of each ocean, the dimensionless overlap integrals discussed in section 4, as well as the integral H_n , defined in section 5.3, which is related to the quadrupole moment of the mode. The ocean depths, mode frequencies, and integrals are all specific to this choice of equation of state and neutron star core density.

4.1.1 Neutron Star Binary and Neutron Star-Black Hole Binary

The initial conditions and orbital motion of BNSs and NSBHs are largely the same when the orbital separation exceeds the diameter of the neutron star. Due to the low mode frequencies of the three neutron star oceans, resonance will occur very early in the inspiral. As such, we consider both BNSs and NSBHs at early times.

For an inspiraling circular binary, the time derivative of the true anomaly $\dot{\Phi}$ is just the orbital frequency

$$\dot{\Phi} = \sqrt{\frac{G(M + M_*)}{D(t)^3}}, \quad (47)$$

where G is the gravitational constant, M is the mass of the neutron star that is tidally perturbed, M_* is the mass of the companion object, and $D(t)$ is the orbital separation as a function of time. The second derivative of the true anomaly is

$$\ddot{\Phi} = -\frac{3}{2}\dot{\Phi}\frac{\dot{D}}{D}, \quad (48)$$

where \dot{D} is the time derivative of D . Due to the emission of GWs, the binary loses energy and $D(t)$ decreases over time. The separation as a function of time $D(t)$ for an inspiraling circular binary is given by (Peters 1964)

$$D(t) = \left(D_0^4 - \frac{256}{5} \frac{G^3 M M_* (M + M_*)}{c^5} t \right)^{1/4}, \quad (49)$$

where D_0 is the orbital separation at time $t = 0$, and c is the speed of light. We have neglected the effects of energy transfer to the neutron star ocean on the orbital motion because, as will be discussed in section 4.2.3, the orbital energy will far exceed the energy transmitted to the ocean mode.

To numerically solve equations 46a and 46b, we must choose values for b^r , b^i , \dot{b}^r , and \dot{b}^i at some initial time from which we start our integration. We use the same initial conditions for circular binary inspirals used by Lai (1994) and start our integration at a time when the binary is very far from merging. These conditions are

$$b^r(0) = \frac{1}{D^{l+1}(\omega^2 - m^2\dot{\Phi}^2)}, \quad (50a)$$

$$\dot{b}^r(0) = \left[-(l+1)\frac{\dot{D}}{D} + \frac{2m^2\dot{\Phi}\ddot{\Phi}}{\omega^2 - m^2\dot{\Phi}^2} \right] b^r(0), \quad (50b)$$

$$b^i(0) = \frac{1}{(\omega^2 - m^2\dot{\Phi}^2)} (2m\dot{\Phi}b^r(0) + m\ddot{\Phi}b^r(0)), \quad (50c)$$

$$\dot{b}^i(0) \approx 0. \quad (50d)$$

We compute b for the $l = 2, m = 0$ and $l = 2, m = 2$ cases, since $m = 2$ and $m = -2$ modes will be equally excited (Lai 1994). We do not compute the $m = \pm 1$ case since $Y_{2\pm 1} = 0$.

4.1.2 Neutron Star Parabolic Encounter

We consider close encounters of neutron stars whose minimum distance of approach is a distance s . Since parabolic orbits correspond to those with an orbital eccentricity of $e = 1$, the orbital separation as a function of radius is

$$D(t) = \frac{2s}{1 + \cos \Phi(t)}, \quad (51)$$

where $\Phi(t)$ here is the true anomaly for a parabolic orbit. Using conservation of angular momentum, we obtain a differential equation for the true anomaly as a function of time

$$\dot{\Phi}(t) = \frac{1}{4} \sqrt{\frac{G(M + M_*)}{s^3}} (1 + \cos \Phi(t))^2. \quad (52)$$

We also obtain the second derivative of the true anomaly $\ddot{\Phi}$ by taking the derivative of $\dot{\Phi}$

$$\ddot{\Phi}(t) = -\frac{1}{2} \sqrt{\frac{G(M + M_*)}{s^3}} (1 + \cos \Phi(t)) \sin \Phi(t) \dot{\Phi}(t). \quad (53)$$

Solving equation 52 gives the true anomaly as a function of time for a parabolic orbit.

Again, we must choose appropriate initial conditions for b^r , b^i , \dot{b}^r , and \dot{b}^i to solve equations 46a and 46b. For a parabolic orbit, the two bodies begin infinitely far away from one another with no speed. Thus, when the companion object is far away from the neutron star, we have $\dot{\Phi}(t) \approx 0$ and $\ddot{\Phi}(t) \approx 0$. When this is the case, $D(t)$ is approximately constant from equation 51, so we obtain a first approximation to b at large distances

$$b \approx \frac{1}{\omega^2 D(t)^{l+1}}. \quad (54)$$

The time derivative \dot{b} becomes

$$\dot{b} \approx -(l+1) \frac{\dot{D}(t)}{D(t)} b, \quad (55)$$

where $\dot{D}(t)$ is the time derivative of orbital separation. Taking the time derivative of equation 55 gives

$$\ddot{b} \approx \left(-(l+1)\frac{\ddot{D}}{D} + (l+2)(l+1)\left(\frac{\dot{D}}{D}\right)^2 \right) b, \quad (56)$$

where \ddot{D} is the second time derivative of orbital separation. We may plug equations 55 and 56 into equation 45 and obtain an expression for b containing initial conditions for both b^r and b^i

$$b \approx \frac{1}{D^{l+1}} \frac{\omega^2 - m^2 \dot{\Phi}^2 + i(m\ddot{\Phi} - 2m(l+1)\dot{\Phi}\frac{\dot{D}}{D})}{\omega^4}, \quad (57)$$

where we have taken only the largest terms. Separating equation 57 into a real and an imaginary part, we get initial conditions valid when $D(t) \gg s$

$$b^r(0) = \frac{1}{\omega^2 D^{l+1}}, \quad (58a)$$

$$\dot{b}^r(0) = -(l+1)\frac{\dot{D}}{D} b^r(0), \quad (58b)$$

$$b^i(0) = \frac{1}{\omega^2} (2m\dot{\Phi}\dot{b}^r(0) + m\ddot{\Phi}b^r(0)), \quad (58c)$$

$$\dot{b}^i(0) \approx 0. \quad (58d)$$

We solve for b in the cases where $l = 2$ and $m = 0$ and $l = 2$ and $m = 2$.

4.2 Tidal Results

We report our results for $a(t)$ for the BNS, NSBH, and NSPE. $a(t)$ is computed by numerically solving equations 46a and 46b for $b(t)$ and substituting $b(t)$ into equation 44. The companion mass used in the BNS and NSPE is $1.25 M_\odot$ and the companion mass used in the NSBH is $20 M_\odot$. We show results for the NSPE when $m = 0$ and the binary inspirals when $m = 2$. The $m = 2$ NSPE tidal amplitude will be significantly weaker than the $m = 0$ amplitude in general because the $m = 2$ case will only generate a large amplitude during a resonant oscillation. Resonant oscillations during NSPEs require very specific initial conditions on the neutron star trajectories, making them less likely to be found in nature. The $m = 0$ binary inspiral cases will also be small compared to the resonant case when $m = 2$. The $m = 0$ case in the binary inspiral corresponds to a static deformation of the neutron star, rather than the larger amplitude resonant oscillation. Resonance of the ocean mode with the tidal force is likely to occur in any isolated binary system containing a neutron star because the system's orbital frequency continuously evolves. We therefore report one tidal response for each possible combination of ocean and companion orbit. Table 2 contains the main quantitative results of this paper.

4.2.1 Resonant Tidal Waves in Binary Inspirals

Both BNS and NSBH inspirals will resonantly excite the ocean modes of their component neutron stars. It is when resonance occurs that the tidal wave achieves its maximum amplitude.

In figure 2, we show the magnitude of the tidal wave amplitudes for both BNSs and NSBHs in the times surrounding resonance. The general evolution of the tidal amplitudes of all three oceans is similar between both BNSs and NSBHs. In the hours leading up

to resonance, the amplitudes of the tidal waves increase by a full order of magnitude. We have not considered any damping mechanisms, although possible mechanisms which can decrease the tidal wave amplitudes include diffusion (Kraav et al. 2021; Dommès & Gusakov 2021), heating (Beloborodov & Li 2016), and GW emission (Lioutas & Stergioulas 2018). Without any damping, the tidal wave will continue to pulsate with the same amplitude following the resonance time. Carbon and oxygen oceans possess tidal wave amplitudes of similar size. The overlap integrals and mode frequencies of these modes are comparable, with carbon oceans having a slightly larger amplitude. In contrast, the amplitudes for the iron oceans are about half that of the other two, as the overlap integral of the iron ocean is about half that of the carbon ocean.

Slight differences between the BNS and NSBH case are apparent. The BNS cases generate slightly higher amplitudes than the NSBH cases because resonance during a BNS occurs when the two bodies are roughly twice as close as during a NSBH. Additionally, the evolution of the tidal wave amplitude and frequency is noticeably slower in the BNS cases. This is a direct consequence of the slower frequency evolution in BNSs.

Ocean tidal waves become resonant with the orbital motion well before merger occurs. We may determine how long before merger these resonances occur from equation 49 by making D_0 the separation of the objects in the binary at resonance time, setting $D(t) = 0$, and solving for t . In BNSs, the carbon ocean reaches resonance with the tidal force ~ 13 years before merger, the oxygen ocean reaches resonance ~ 15 years before merger, and the iron ocean reaches resonance ~ 33 years before merger. In NSBHs, the carbon ocean reaches resonance ~ 1.5 years before merger, the oxygen ocean reaches resonance ~ 1.8 years before merger, and the iron ocean reaches resonance ~ 4 years before merger. Thus any emission from the resonant ocean tides would well precede the compact binary mergers.

4.2.2 Tidal Waves Excited by Parabolic Encounters

Parabolic encounters between neutron stars will excite tidal waves in neutron star oceans when the neutron stars are at their distance of closest approach. When this occurs, the tidal force of the companion star provides an impulse to the ocean, causing it to pulsate. In this paper, we quote results when the closest distance of approach is $s = 6.4 \times 10^6$ cm. This is the distance of closest approach where the carbon ocean tidal wave amplitude $a(t)$ in an NSPE is approximately equal to that of a BNS. For different values of s , the amplitudes of the excited tidal waves will scale our results by a factor of $(s/6.4 \times 10^6 \text{ cm})^{-3}$. Figure 3 shows the tidal wave amplitudes in the times surrounding an NSPE for the three oceans.

After the NSPE occurs, the tidal waves will oscillate with the mode frequency of the ocean mode. The amplitudes are approximately the same order for each of the three oceans we consider. As in the binary inspiral cases, the iron ocean has the smallest amplitude. The distance of closest approach in this NSPE is about two orders of magnitude smaller than the resonance distance in the binary inspiral case. NSPEs require much closer encounters than NSBHs and BNSs to produce sizable ocean tidal waves.

We estimate the event rate for NSPEs within this nominal encounter distance inside a globular cluster. NSPE event rates have been computed in previous works (Kocsis et al. 2006; Tsang 2013), but not for these very small encounter distances. We estimate the event rate of NSPEs in a globular cluster as

$$\nu_{NSPE} = \frac{1}{2} N_{NS} n_{NS} v_0 \sigma_{NSPE}, \quad (59)$$

Ocean	Carbon	Oxygen	Iron
Energy deposited in BNS (erg)	7.9×10^{45}	4.3×10^{44}	3.5×10^{39}
Time before BNS merger (yr)	13	15	33
Energy deposited in NSBH (erg)	3.6×10^{45}	2.0×10^{44}	1.6×10^{39}
Time before NSBH merger (yr)	1.5	1.8	4
Energy deposited in NSPE where $s = 6.4 \times 10^6$ cm (erg)	4.1×10^{45}	2.3×10^{44}	2.1×10^{39}
Time before NSPE (s)	0	0	0

Table 2. The main quantitative results of this paper for the three neutron star oceans and three tidal scenarios considered. This table includes the energy deposited into each ocean due to the tide and the time at which this energy is deposited.

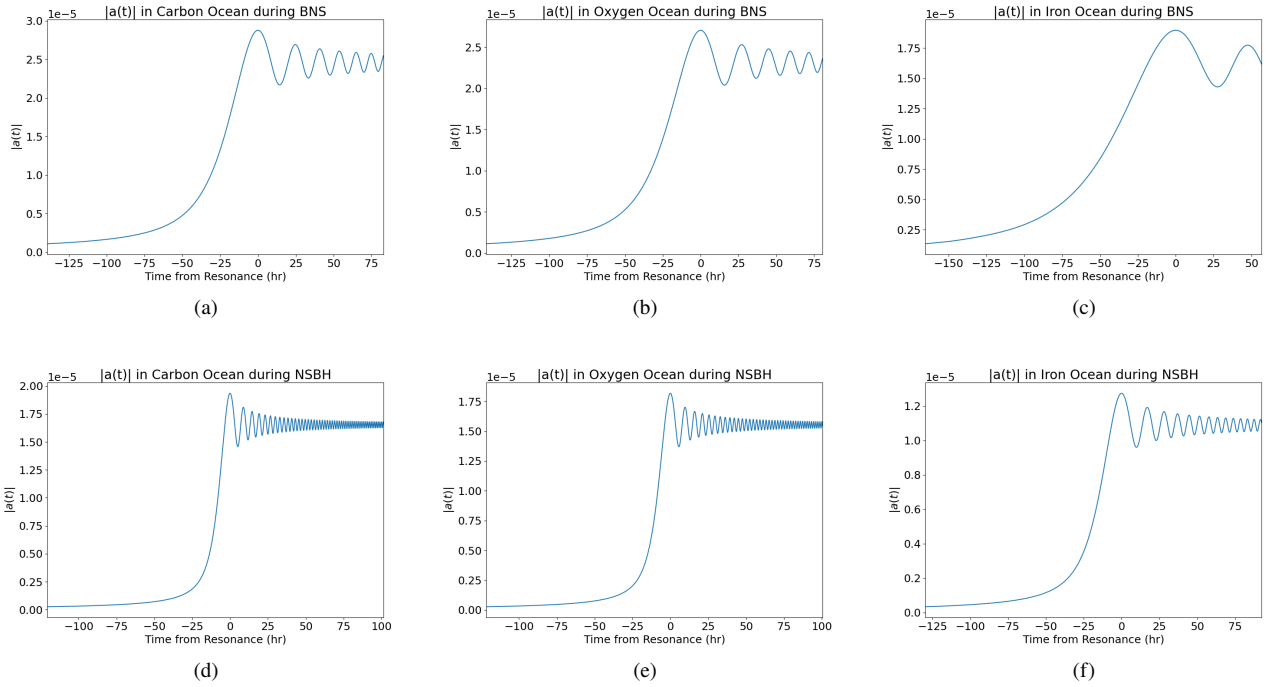


Figure 2. The magnitudes of the dimensionless resonant ocean tidal wave amplitude $|a(t)|$ during compact binary inspirals as a function of time without damping. The horizontal axis shows the time from resonance in hours and the vertical axis shows $|a(t)|$. The top row shows tidal wave amplitudes during a BNS (a) in a carbon ocean, (b) in an oxygen ocean, and (c) in an iron ocean. The bottom row shows tidal wave amplitudes during an NSBH (d) in a carbon ocean, (e) in an oxygen ocean, and (f) in an iron ocean.

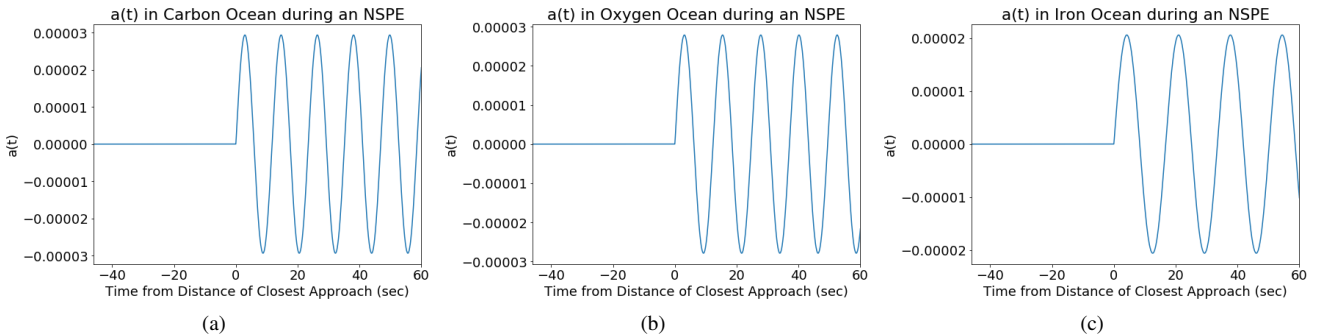


Figure 3. The real part of the dimensionless ocean tidal wave amplitude $a(t)$ during an NSPE as a function of time without damping. The horizontal axis shows the time from resonance in seconds and the vertical axis shows $a(t)$. The sharp increase in the tidal wave height at time $t = 0$ is due to the impulse from the neutron stars reaching their smallest orbital separation. (a) shows tidal wave amplitudes in a carbon ocean, (b) shows the tidal wave amplitude in an oxygen ocean, and (c) shows the tidal wave amplitude in an iron ocean.

where N_{NS} is the number of neutron stars in a globular cluster, n_{NS} is the number density of neutron stars in a globular cluster, $v_0 = \sqrt{\frac{G(M+M_*)}{s}}$ is the relative speed of neutron stars in an NSPE at the periastron distance, and σ_{NSPE} is the cross-section of NSPEs. Note that in this expression for event rate, we use the relative velocity between neutron stars at periastron, while [Kocsis et al. \(2006\)](#) use the relative velocity at infinite separation v_∞ . We use the velocity at periastron because we are considering parabolic orbits where $v_\infty = 0$. The cross section will be

$$\sigma_{NSPE} = \pi s^2, \quad (60)$$

for the encounter distance s . The event rate for NSPEs within a distance s becomes

$$\nu_{NSPE} = \frac{1}{2} \frac{N_{NS}^2}{\frac{4}{3}\pi R_{GC}^3} \sqrt{G(M+M_*)s^3}, \quad (61)$$

where we have assumed the number density of neutron stars in a globular cluster is uniform such that $n_{NS} = \frac{N_{NS}}{\frac{4}{3}\pi R_{GC}^3}$ with R_{GC} being the radius of the globular cluster. Using $N_{NS} = 500$, $R_{GC} = 1$ pc as was done by [Kocsis et al. \(2006\)](#), and $M = M_* = 1.25 M_\odot$, we find $\nu_{NSPE} = 1.03 \times 10^{-20} \text{ yr}^{-1}$. These events are therefore extremely rare.

Despite the rarity of these events, their tidal waves are generated in exact coincidence with the time of the closest passage of the neutron stars, so observation of emission from such tides can exactly demarcate the time of closest passage.

4.2.3 Energetics of Ocean Tidal Waves

We now compute the energy deposited into the ocean modes during the tidal excitations previously discussed. The energy of an oscillation mode can be broken up into potential and kinetic energy. The kinetic energy and potential energy are ([Lai 1994](#))

$$E_k = \frac{1}{2} \int \rho \frac{\partial \vec{\xi}}{\partial t} \cdot \frac{\partial \vec{\xi}^*}{\partial t} dV = \frac{1}{2} |\dot{a}(t)|^2 A_n^2, \quad (62a)$$

$$E_p = \frac{1}{2} \int \rho \omega_n^2 \vec{\xi} \cdot \vec{\xi}^* dV = \frac{1}{2} \omega_n^2 |a(t)|^2 A_n^2. \quad (62b)$$

In binary inspirals after resonance, the kinetic energy and the potential energy should be equal to one another. Additionally, both the $m = 2$ and $m = -2$ modes contribute to the energy equally. Therefore, the total energy deposited into each mode from the tidal interaction will be ([Lai 1994](#))

$$E = \omega_n^2 |a_{n,max}|^2 A_n^2, \quad (63)$$

where $|a_{n,max}|$ is the maximum amplitude of the tidal wave. In the NSPE case, since we are considering only the $m = 0$ case, there is just one contribution. The NSPE total energy will be half of the energy of a binary inspiral of the same amplitude ([Lai 1994](#)).

We compute the energy deposited into the ocean after tidal resonance during a BNS inspiral to be $\sim 7.9 \times 10^{45}$ erg in a carbon ocean, $\sim 4.3 \times 10^{44}$ erg in an oxygen ocean, and $\sim 3.5 \times 10^{39}$ erg in an iron ocean. Similarly, we compute the energy deposited into the ocean after tidal resonance during an NSBH inspiral to be $\sim 3.6 \times 10^{45}$ erg in a carbon ocean, $\sim 2.0 \times 10^{44}$ erg in an oxygen ocean, and 1.6×10^{39} erg in an iron ocean. The orbital energy at the time of resonance is $\gtrsim 10^{50}$ erg, thus justifying our assumption that the orbital motion remains unaffected.

We compute the energy deposited into the ocean after an NSPE

whose distance of closest approach is $s = 6.4 \times 10^6$ cm to be 4.1×10^{45} erg for carbon oceans, 2.3×10^{44} erg for oxygen oceans, and 2.1×10^{39} erg for iron oceans. For different values of s , these energy results will scale by $(s/6.4 \times 10^6 \text{ cm})^{-6}$.

5 DISCUSSION

We have determined that tidal waves in neutron star oceans can be generated during BNS inspirals, NSBH inspirals, and NSPEs, and quantitatively estimated their amplitudes, energies, and timing. The tidal waves in each of these systems have unique properties. In binary inspirals, the neutron star ocean mode becomes resonant with the tidal force of the companion years before coalescence. Conversely, the impulsive tidal force during an NSPE excites the ocean mode at the moment of closest approach. The impulse generates simple continuous oscillatory tidal waves with the frequency of the neutron star ocean mode. The implications of these results extend to multi-messenger astronomy and neutron star geophysics.

5.1 Ocean Tidal Waves as Compact Binary Merger Precursor Flares and Parabolic Encounter Multi-Messenger Sources

Dynamical activity in neutron star oceans has been considered as a potential emitter of neutrino and electromagnetic radiation ([Reisenegger & Goldreich 1994](#); [Heyl 2004](#); [Deibel 2016](#); [Wang et al. 2021](#)). Neutron star oscillations have been observed in relation to electromagnetic bursts ([Strohmayer & Mahmoodifar 2014](#)). Therefore, the tidal waves in neutron star oceans during a binary inspiral might correspond to multi-messenger emission due to the energy deposited. We hypothesize that resonant ocean tidal waves in neutron stars may be a new source of precursor emission to compact binary mergers during the early inspiral.

The energies deposited into the ocean modes after resonance (computed in section 4.2.3) may serve as estimates for the energy available for these flares. Thus, $\sim 10^{39} - 10^{45}$ erg are available to source resonant ocean tidal flares. We have neglected the presence of the neutron star magnetic field; however, the interaction between the excited ocean and the surface magnetic field may serve as a channel for generating electromagnetic emission from the excited ocean. Because neutron star surfaces also emit thermal neutrinos ([Yakovlev & Pethick 2004](#), e.g.), it is possible that this emission is manifest in neutrinos. In the remainder of this paper, we will limit our discussion to accompanying electromagnetic emission.

Pre-existing mechanisms for causing precursor flares before compact binary mergers include the interactions of neutron star magnetospheres in a BNS ([Ascenzi et al. 2021](#)), orbital motion of a weakly magnetized companion and a highly magnetized neutron star in either a BNS or NSBH ([Vietri 1996](#); [Hansen & Lyutikov 2001](#); [McWilliams & Levin 2011](#); [Lai 2012](#); [Piro 2012](#); [Sridhar et al. 2021](#)), and the tidally induced cracking of a neutron star crust during a BNS or NSBH ([Suvorov & Kokkotas 2020](#); [Gittins et al. 2020](#); [Passamonti et al. 2021](#); [Kuan et al. 2021c,a](#)). Precursor flares from previously considered channels are only expected just before a merger ($\lesssim 10$ s) ([Mathews & Wilson 1997](#); [Sridhar et al. 2021](#); [Passamonti et al. 2021](#)).

In contrast to these other mechanisms, precursor flares associated with resonant neutron star ocean tidal waves could be excited years or decades before the merger when resonance occurs (~ 1 yr for NSBHs and ~ 10 yr for BNSs). Resonant ocean tidal flares can therefore be very early warning signs of compact binary mergers

involving neutron stars. Notably, NSBHs should have little trouble emitting early flares since the black hole will be too far from the neutron star to absorb all the emission. Early warning precursor flares can be additional messengers for studying BNS and NSBH systems and neutron stars more generally. The number of years before merger will provide information about both the type of merger and the material in neutron star oceans. In fact, the delay between flare and merger can distinguish these qualities. To observe these flares from compact binary mergers in practice, one will likely need to retroactively search data from electromagnetic detectors coincident in sky localization with compact binary mergers observed by GW detectors. The use of space-based GW detectors such as LISA (Amaro-Seoane et al. 2017) may assist in identifying the flares in advance of mergers as space-based detectors will detect GWs from compact binary inspirals well before mergers at galactic distances (LISA Study Team et al. 2000; Robson et al. 2019). Observations of resonant ocean tidal flares from compact binary inspirals will complement multi-messenger efforts to observe these exotic systems and their oceans.

Additionally, these same flares may be generated in NSPEs as energy is also deposited into the ocean in these systems. The ignition of the tidal wave would be precisely coincident with the NSPE. As such, coincident detections of the broadband GW bursts generated by the orbital motion (Turner 1977a; Kovacs & Thorne 1978; Kocsis et al. 2006; De Vittori et al. 2012) and tidally induced electromagnetic flares can manifest in multi-messenger observations that allow for the study of NSPEs and their constituent neutron stars.

5.2 Detection of Electromagnetic Flares from Neutron Star Ocean Tidal Waves

We posit two possible scenarios for electromagnetic flares originating from neutron star ocean tidal waves and qualitatively discuss the detection of these flares. Since the mode frequencies of the oceans studied are on the order of tens of mHz, it is possible that the electromagnetic radiation from neutron star ocean tides is in the ultra low frequency regime. As of this paper's writing, detection of ultra low frequency electromagnetic radiation on geophysical scales has been considered (Grimm 2002; Grimm et al. 2009; Kozakiewicz et al. 2016), but no astronomical electromagnetic instrument capable of tapping frequencies below ~ 0.001 MHz has been proposed (Bergman et al. 2009; Saks et al. 2010; Blott et al. 2013; Boonstra et al. 2016; Cecconi et al. 2018; Belov et al. 2018; Prinsloo et al. 2018; Rajan et al. 2016; Bentum et al. 2020). Therefore, it would be extremely difficult to detect mHz radiation from neutron star ocean tidal waves.

However, due to complicated micro-physics and the large amount of energy deposited into the neutron star ocean, we propose that neutron star ocean tides may produce high-energy electromagnetic radiation in the gamma ray or X-ray regime with spectra and time-scales similar to that of soft-gamma repeaters (SGRs) or type-I X-ray bursts, perhaps through interactions between the surface magnetic field and the ocean. Due to the hot temperatures of neutron star surfaces, thermal emission of X-rays may be a particularly compelling manifestation of this emission. Since we have considered hot neutron stars with $T = 10^8$ K at the crust, these neutron stars may already be accreting and emitting X-rays thermally. The tidal resonance will impart additional energy into the neutron star ocean, which we suppose may increase the flux of photons on timescales comparable to the period of the computed ocean mode. We note that accretion requires a non-compact companion to sup-

ply the material. We have neglected the effects of such additional companions for simplicity.

Taking the flare conjecture at face-value and assuming the energy deposited into the ocean from the tide is isotropically expelled as either gamma rays or X-rays, we estimate how far away a resonant neutron star ocean tidal flare can be detected by the gamma ray detector Fermi (Atwood et al. 2009) and X-ray telescopic array NuSTAR (Harrison et al. 2013).

We estimate the photon flux from such a flare assuming all emission is in either the X-ray or gamma ray spectrum. Taking R to be the distance between a detector and the source, we approximate the photon flux at the detector as

$$F_\gamma \approx \frac{E}{E_\gamma} \frac{\omega}{4\pi R^2}, \quad (64)$$

where E is the energy of the ocean tidal wave, E_γ is the energy of a photon, and ω is the mode frequency. We have assumed that all energy deposited into the mode is radiated away into a flare on a timescale comparable to the inverse of the mode frequency ω as it is the only short timescale we have.

For Fermi, we estimate the furthest distance at which such a flare could be observed as

$$R \approx \sqrt{\frac{E}{E_\gamma} \frac{\omega}{4\pi F_t}}, \quad (65)$$

where F_t is the photon flux threshold for Fermi. The photon flux threshold of Fermi is $0.74 \text{ photons cm}^{-2} \text{ s}^{-1}$ in the range of 8 keV to 40 MeV (Atwood et al. 2009).

For short duration X-ray sources, NuSTAR's sensitivity is limited by photon statistics. The signal to noise ratio (SNR) for a short-duration flare assuming all photons are at the same energy is

$$K = \sqrt{F_\gamma T \mathcal{A}}, \quad (66)$$

where T is the duration of the flare and \mathcal{A} is the effective area of NuSTAR. Substituting in our estimate for F_γ and taking $T \approx \omega^{-1}$, the SNR becomes

$$K \approx \sqrt{\frac{E}{E_\gamma} \frac{\mathcal{A}}{4\pi R^2}}. \quad (67)$$

We estimate the furthest distance at which a flare can be observed by NuSTAR as

$$R \approx \frac{1}{K} \sqrt{\frac{E}{E_\gamma} \frac{\mathcal{A}}{4\pi}}, \quad (68)$$

for some SNR threshold K . Notice that ω has dropped out of equation 68, so this estimate is independent of the precise timescale of the flare as long as it is a short-duration flare (Harrison et al. 2013). The effective area of NuSTAR is approximately 800 cm^2 for photon energies of 6 – 10 keV and 300 cm^2 for photon energies of 10 – 30 keV (Harrison et al. 2013). We take an SNR threshold of $K = 5$.

We compute the distances for each ocean and binary inspiral case for four detection scenarios: resonant ocean tidal flare photons are 1) gamma rays with $E_\gamma = 40$ MeV detected by Fermi, 2) X-rays with $E_\gamma = 8$ keV detected by Fermi, 3) higher energy X-rays with $E_\gamma = 20$ keV detected by NuSTAR, and 4) lower energy X-rays with $E_\gamma = 8$ keV detected by NuSTAR. We quote our results in table 3. We find that if the emission from resonant ocean tidal flares is in the gamma ray spectrum or if crusts are composed of iron, Fermi and NuSTAR will have almost no capability to detect flares of extragalactic compact binaries, the main sources of interest

for ground-based GW detectors. Excitingly, however, if resonant ocean tidal flares are emitted in the X-ray spectrum in carbon or oxygen oceans, both NuSTAR and Fermi will have the ability to detect them out to distances on the orders of $\sim 10 - 100$ Mpc, which coincide with the BNS ranges of currently operational GW detectors (The LIGO Scientific Collaboration et al. 2021a). In fact, BNS and NSBH inspirals have been observed out to a few 100 Mpc (LIGO Scientific Collaboration & Virgo Collaboration 2019; The LIGO Scientific Collaboration & the Virgo Collaboration 2021; The LIGO Scientific Collaboration et al. 2021a).

We may crudely estimate an optimistic event rate for these flares using the estimated merger rates of BNSs and NSBHs from LIGO-Virgo-KAGRA's third GW catalog (The LIGO Scientific Collaboration et al. 2021b). The 90% credible interval for the merger rates is reported as $10 - 1700 \text{ Gpc}^{-3} \text{ yr}^{-1}$ for BNSs and $7.8 - 140 \text{ Gpc}^{-3} \text{ yr}^{-1}$ for NSBHs (The LIGO Scientific Collaboration et al. 2021b; Mandel & Broekgaarden 2022). Assuming the case of a flare detectable out to ~ 100 Mpc, we estimate the event rates for detectable resonant ocean tidal flares by multiplying a spherical volume with radius 100 Mpc by the quoted merger rates. The event rates would be $\sim 0.04 - 7 \text{ yr}^{-1}$ for BNSs and $\sim 0.03 - 0.6 \text{ yr}^{-1}$ for NSBHs. Therefore, with long enough observation time, precursor flares associated with resonant ocean tidal waves in compact binary inspirals may be detectable as multi-messenger emissions.

5.3 Gravitational Waves from Neutron Star Ocean Tidal Waves

Due to the time dependent perturbation to the mass density, tidal pulsations in compact stars should also generate GWs (Turner 1977b). We now investigate the GWs produced by neutron star ocean tidal waves. The GW metric h_{ij}^{TT} can be written as a multipole expansion (Turner 1977b)

$$h_{ij}^{TT} = \frac{G}{Rc^4} \sum_{l,m} B_{lm} \left(t - \frac{R}{c} \right) T_{ij}^{lm}(\theta, \phi), \quad (69)$$

where G is the gravitational constant, c is the speed of light, $B_{lm}(t - \frac{R}{c})$ is a time-dependent amplitude evaluated at the retarded time with dimensions of the second time derivative of the mass quadrupole moment, and T_{ij}^{lm} are transverse-traceless tensor spherical harmonics (Turner 1977b,a). As we have done throughout this work, we restrict ourselves to the $l = 2$ harmonic. For an oscillation mode that generates small perturbations in the mass density, B_{lm} is (Turner 1977b)

$$B_{2m}(t) = \frac{16\pi}{5\sqrt{3}} \frac{d^2}{dt^2} \int \delta\rho Y_{2m}^* r^2 dV, \quad (70)$$

where $\delta\rho$ is the Eulerian perturbation to the mass density. Rearranging equation 9, we obtain an expression for the Eulerian perturbation

$$\delta\rho = -\nabla \cdot (\rho \vec{\xi}) = -a(t) \left(U \frac{d\rho}{dr} + \rho \left(\frac{dU}{dr} + \frac{2U}{r} - l(l+1) \frac{V}{r} \right) \right) Y_{lm}. \quad (71)$$

Substituting equation 71 into equation 70 gives

$$B_{2m}(t) = \frac{16\pi}{5\sqrt{3}} \ddot{a}(t) H_n, \quad (72)$$

where we have defined an integral H_n as

$$H_n = - \int \left(U \frac{d\rho}{dr} + \rho \left(\frac{dU}{dr} + \frac{2U}{r} - l(l+1) \frac{V}{r} \right) \right) r^4 dr, \quad (73)$$

which quantifies an oscillation mode's ability to generate GWs. Note that the only time dependence in equation 72 arises from \ddot{a} .

We obtain results for the integral H_n for each of our three ocean models. These are displayed in table 1 in units of g cm^2 . Like other integrals computed, H_n is largest in carbon oceans because the carbon ocean is the largest.

We approximate the GW strain $h(t)$ in a GW detector from neutron star ocean tidal waves as

$$h(t) \approx \frac{G}{Rc^4} \frac{16\pi}{5\sqrt{3}} \ddot{a}(t) H_n. \quad (74)$$

We determine at what distance R there would be GW signals with amplitudes $h \sim 10^{-20}$. This is approximately the smallest amplitude detectable with current space-based GW detector technology (LISA Study Team et al. 2000; Robson et al. 2019). We find that GWs from none of the configurations considered will be able to escape the immediate vicinity of the neutron star. The configuration which generates the largest GWs is a carbon ocean during a BNS inspiral. The distance from the ocean at which the GWs have an amplitude of $\sim 10^{-20}$ is ~ 200 km. In contrast, the smallest GWs are generated in an iron ocean during an NSBH inspiral. In this case, the GW amplitude is $\sim 10^{-20}$ only ~ 30 cm away. This makes detecting GWs from neutron star ocean tides virtually impossible. While these GWs will serve as a source of extremely weak damping, we find that the damping timescales are longer than the age of the universe and will thus not impact neutron star ocean tides.

Despite GWs from the ocean tidal waves being undetectable, BNSs, NSBHs, and NSPEs all emit GWs due to their orbital motion. During the early inspiral of BNSs and NSBHs, GWs will be detectable by LISA (LISA Study Team et al. 2000; Robson et al. 2019). GWs from BNS and NSBH mergers are already detected by ground-based GW detectors (LIGO Scientific Collaboration & Virgo Collaboration 2017; LIGO Scientific Collaboration et al. 2021). Consequently, joint detection of GWs with resonant ocean tidal flares remains a possibility for multi-messenger astrophysics.

6 CONCLUSION

Neutron star oceans can sustain resonant tides. Though rather small in height due to the extreme gravity on the surface of the neutron star, the tidal waves excited in compact binary inspirals and in parabolic encounters possess large amounts of energy. In our phenomenological unmagnetized and non-rotating model, ocean tidal waves can have energies in the range of $10^{39} - 10^{45}$ erg, depending on the element that composes the neutron star crust. This energy, coupled with the rotational and magnetic energy of a real neutron star, has the potential to serve as the fuel for electromagnetic flares. Such electromagnetic flares could become very early warning signs of NSBH (~ 1 yr before merger) and BNS (~ 10 yr before merger) mergers and tools to study neutron star oceans. Distinct signatures of these flares could be their timing relative to compact binary mergers, as well as their durations and oscillation periods, which should both be related to the period of the neutron star ocean mode. Higher frequency ocean g-modes in particular may provide oscillations in resonant ocean tidal flares. More work is needed to understand the physical mechanisms which can release the energy for flares as well as the effects of rotation and magnetization.

We find that neutron star ocean resonant tidal flares, if emitted in the form of X-rays, may be detected out to distances as far as a few 10–100 Mpc with Fermi and NuSTAR, comparable to the distances of BNS and NSBH mergers observed by GW detectors. We find that

Ocean	Carbon	Oxygen	Iron
BNS Gamma Ray with Fermi (Mpc)	1.2	0.28	0.00078
BNS X-Ray with Fermi (Mpc)	83	20	0.055
BNS Higher energy X-Ray with NuSTAR (Mpc)	160	37	0.10
BNS Lower energy X-Ray with NuSTAR (Mpc)	400	95	0.27
NSBH Gamma Ray with Fermi (Mpc)	0.79	0.19	0.00053
NSBH X-Ray with Fermi (Mpc)	56	13	0.037
NSBH Higher energy X-Ray with NuSTAR (Mpc)	110	25	0.070
NSBH Lower energy X-Ray with NuSTAR (Mpc)	270	64	0.18

Table 3. The estimated distances (in Mpc) out to which flares from neutron star oceans could be detected with Fermi or NuSTAR assuming isotropic emission. For Fermi, X-ray distances are computed assuming $E_\gamma = 8$ keV, while gamma ray distances are computed assuming $E_\gamma = 40$ MeV. For NuSTAR, the lower energy X-ray distances are computed assuming $E_\gamma = 8$ keV, while the higher energy X-ray distances are computed assuming $E_\gamma = 20$ keV.

X-ray emission could have detection rates as high as $\sim 7 \text{ yr}^{-1}$ for BNSs and $\sim 0.6 \text{ yr}^{-1}$ for NSBHs. Neutron star ocean tides are consequently a possible source of emission which can accompany observable GWs. Additional future direction may involve reviewing past NuSTAR and Fermi data for X-ray bursts in coincident angular locations of observed BNS and NSBH mergers.

Neutron star ocean tides and oscillations may contribute to future multi-messenger observations of astrophysical compact binary mergers and neutron stars. From the timing of resonant neutron star ocean tides as compared with other forms of astrophysical emission, we can learn about compact binaries and neutron star oceans. Future studies into ocean tidal waves on top of crustal mountains (Gittins et al. 2021; Gittins & Andersson 2021) and resultant neutron star ocean tsunamis may also yield interesting results. More exotic systems including collisions between neutron stars and planets may also produce ocean activity that results in multi-messenger emission. Multi-messenger emission of neutron stars, with the addition of emission from ocean tidal waves, will contain essential information about the enigmatic but rich dynamics of neutron stars and their interior structure, probing the geophysics of these objects.

ACKNOWLEDGMENTS

The authors are grateful for very helpful discussions with Nils Andersson, Fabian Gittins, Péter Petreczky, and Charles Hailey. The authors thank Nils Andersson, Péter Petreczky, and Charles Hailey for reviewing the manuscript and providing constructive feedback. The authors thank Columbia University in the City of New York and the University of Florida for their generous support. The Columbia Experimental Gravity group is grateful for the generous support of Columbia University. A.S. is grateful for the support of the Columbia College Science Research Fellows program and the Heinrich, CC Summer Research Fellowship. L.A. is grateful for the Columbia Undergraduate Scholars Program Summer Enhancement Fellowship and the Columbia Center for Career Education Summer Funding Program. G.S. is grateful for the generous support of the Columbia University Department of Mathematics Research Experience for Undergraduates program. I.L. is grateful for the generous support of the Columbia University Amgen Scholars program. I.B. acknowledges the support of the Alfred P. Sloan Foundation and NSF grants PHY-1911796 and PHY-2110060.

DATA AVAILABILITY

The data underlying this article will be shared on reasonable request to the corresponding author.

REFERENCES

- Aasi J., et al., 2015, *ApJ*, **813**, 39
- Abbott B. P., others KAGRA Collaboration LIGO Scientific Collaboration VIRGO Collaboration 2018, *Living Reviews in Relativity*, **21**, 3
- Abbott B. P., et al., 2019, *Physical Review X*, **9**, 011001
- Abbott R., et al., 2022, *Phys. Rev. D*, **105**, 082005
- Acernese F., et al., 2015, *Classical and Quantum Gravity*, **32**, 024001
- Akutsu T., et al., 2019, *Classical and Quantum Gravity*, **36**, 165008
- Alsing J., Silva H. O., Berti E., 2018, *MNRAS*, **478**, 1377
- Amaro-Seoane P., et al., 2017, arXiv e-prints, p. [arXiv:1702.00786](https://arxiv.org/abs/1702.00786)
- Andersson N., 2021, *Universe*, **7**, 97
- Andersson N., Kokkotas K. D., 1998, *MNRAS*, **299**, 1059
- Andersson N., Pnigouras P., 2020, *Phys. Rev. D*, **101**, 083001
- Antoniadis J., Tauris T. M., Ozel F., Barr E., Champion D. J., Freire P. C. C., 2016, arXiv e-prints, p. [arXiv:1605.01665](https://arxiv.org/abs/1605.01665)
- Ascenzi S., Oganesyan G., Branchesi M., Ciolfi R., 2021, *Journal of Plasma Physics*, **87**, 845870102
- Atwood W. B., et al., 2009, *ApJ*, **697**, 1071
- Bae Y.-B., Kim C., Lee H. M., 2014, *MNRAS*, **440**, 2714
- Baiko D. A., Chugunov A. I., 2018, *MNRAS*, **480**, 5511
- Bandari A., 2014, Master's thesis, California State University, Long Beach
- Bartos I., Marka S., 2019, *Nature*, **569**, 85
- Belczynski K., et al., 2018, *A&A*, **615**, A91
- Beloborodov A. M., Li X., 2016, *ApJ*, **833**, 261
- Belov K., et al., 2018, *Experimental Astronomy*, **46**, 241
- Bentum M. J., et al., 2020, *Advances in Space Research*, **65**, 856
- Bergman J. E. S., Blott R. J., Forbes A. B., Humphreys D. A., Robinson D. W., Stavrinidis C., 2009, arXiv e-prints, p. [arXiv:0911.0991](https://arxiv.org/abs/0911.0991)
- Bildsten L., Cutler C., 1995, *ApJ*, **449**, 800
- Bildsten L., Ushomirsky G., Cutler C., 1996, *ApJ*, **460**, 827
- Bilous A. V., Watts A. L., 2019, *ApJS*, **245**, 19
- Blott R. J., et al., 2013, in European Planetary Science Congress. pp EPSC2013-279
- Boonstra A.-J., et al., 2016, in 2016 IEEE Aerospace Conference. pp 1–20
- Brown E. F., Cumming A., 2009, *ApJ*, **698**, 1020
- Brown E. F., Bildsten L., Rutledge R. E., 1998, *ApJ*, **504**, L95
- Bult P., et al., 2021, *ApJ*, **907**, 79
- Cecconi B., et al., 2018, in EGU General Assembly Conference Abstracts. EGU General Assembly Conference Abstracts. p. 3648 ([arXiv:1710.10245](https://arxiv.org/abs/1710.10245))
- Chambers F. R. N., Watts A. L., 2020, *MNRAS*, **491**, 6032
- Chambers F. R. N., Watts A. L., Cavecchi Y., Garcia F., Keek L., 2018, *MNRAS*, **477**, 4391
- Chamel N., Haensel P., 2008, *Living Reviews in Relativity*, **11**, 10

- Chandrasekhar S., 1957, An introduction to the study of stellar structure. Vol. 2, Courier Corporation
- Chatzizoannou K., 2020, *General Relativity and Gravitation*, 52, 109
- Chornock R., et al., 2017, *ApJ*, 848, L19
- Cowling T. G., 1941, *MNRAS*, 101, 367
- Cowperthwaite P. S., et al., 2017, *ApJ*, 848, L17
- De Vittori L., Jetzer P., Klein A., 2012, *Phys. Rev. D*, 86, 044017
- Deibel A., 2016, *ApJ*, 832, 44
- Dommes V. A., Gusakov M. E., 2021, *Phys. Rev. D*, 104, 123008
- Dziembowski W. A., 1971, *Acta Astron.*, 21, 289
- Farouki R. T., Hamaguchi S., 1993, *Phys. Rev. E*, 47, 4330
- Ferrari V., 2010, *Classical and Quantum Gravity*, 27, 194006
- Ferrari L., Rossi P. C. R., Malheiro M., 2010, *International Journal of Modern Physics D*, 19, 1569
- Friedman J. L., Schutz B. F., 1978, *ApJ*, 221, 937
- Fujimoto M. Y., Hanawa T., Iben I. J., Richardson M. B., 1984, *ApJ*, 278, 813
- Galloway D. K., Muno M. P., Hartman J. M., Psaltis D., Chakrabarty D., 2008, *ApJS*, 179, 360
- Geroyannis V. S., Tzelati E. E., Karageorgopoulos V. G., 2017, *International Journal of Modern Physics C*, 28, 1750080
- Gittins F., Andersson N., 2021, *MNRAS*, 507, 116
- Gittins F., Andersson N., Pereira J. P., 2020, *Phys. Rev. D*, 101, 103025
- Gittins F., Andersson N., Jones D. I., 2021, *MNRAS*, 500, 5570
- Grimm R. E., 2002, *Journal of Geophysical Research (Planets)*, 107, 5006
- Grimm R. E., Berdanier B., Warden R., Harrer J., Demara R., Pfeiffer J., Blohm R., 2009, *Planet. Space Sci.*, 57, 1268
- Haensel P., Zdunik J. L., 1990, *A&A*, 227, 431
- Haensel P., Zdunik J. L., 2003, *A&A*, 404, L33
- Haensel P., Zdunik J. L., 2008, *A&A*, 480, 459
- Haensel P., Potekhin A. Y., Yakovlev D. G., 2007, *Neutron Stars 1: Equation of State and Structure*. Vol. 326
- Hansen B. M. S., Lyutikov M., 2001, *MNRAS*, 322, 695
- Hansen C. J., van Horn H. M., 1975, *ApJ*, 195, 735
- Harrison F. A., et al., 2013, *ApJ*, 770, 103
- Haskell B., 2015, *International Journal of Modern Physics E*, 24, 1541007
- Heyl J. S., 2004, *ApJ*, 600, 939
- Ho W. C. G., Lai D., 1999, *MNRAS*, 308, 153
- Horowitz C. J., Kadau K., 2009, *Phys. Rev. Lett.*, 102, 191102
- Jackson J. D., 1962, *Classical Electrodynamics*
- Kocsis B., Gáspár M. E., Márka S., 2006, *ApJ*, 648, 411
- Kovacs S. J. J., Thorne K. S., 1978, *ApJ*, 224, 62
- Kozakiewicz J., Kulak A., Kubisz J., Zietara K., 2016, *Earth Moon and Planets*, 118, 103
- Kraav K. Y., Gusakov M. E., Kantor E. M., 2021, *MNRAS*, 506, L74
- Krüger C. J., Kokkotas K. D., Manoharan P., Völkel S. H., 2021, *Frontiers in Astronomy and Space Sciences*, 8, 166
- Kuan H.-J., Suvorov A. G., Kokkotas K. D., 2021a, *MNRAS*,
- Kuan H.-J., Suvorov A. G., Kokkotas K. D., 2021b, arXiv e-prints, p. arXiv:2107.00533
- Kuan H.-J., Suvorov A. G., Kokkotas K. D., 2021c, *MNRAS*, 506, 2985
- Kuan H.-J., Suvorov A. G., Kokkotas K. D., 2021d, *MNRAS*, 508, 1732
- LIGO Scientific Collaboration 2015, *Classical and Quantum Gravity*, 32, 074001
- LIGO Scientific Collaboration Virgo Collaboration 2017, *Phys. Rev. Lett.*, 119, 161101
- LIGO Scientific Collaboration Virgo Collaboration 2019, *Physical Review X*, 9, 031040
- LIGO Scientific Collaboration VIRGO Collaboration KAGRA Collaboration 2021, *ApJ*, 915, L5
- LISA Study Team et al., 2000, *ESA System and Technology Study Report ESA-SCI*, 11
- Lai D., 1994, *MNRAS*, 270, 611
- Lai D., 2012, *ApJ*, 757, L3
- Lattimer J. M., Prakash M., 2001, *ApJ*, 550, 426
- Lau H. K., Leung P. T., Lin L. M., 2010, *The Astrophysical Journal*, 714, 1234–1238
- Ledoux P., 1974, in Ledoux P., Noels A., Rodgers A. W., eds, Vol. 59, *Stellar Instability and Evolution*. p. 135
- Lee U., 2004, *ApJ*, 600, 914
- Lioutas G., Stergioulas N., 2018, *General Relativity and Gravitation*, 50, 12
- Ma S., Yu H., Chen Y., 2021, *Phys. Rev. D*, 103, 063020
- Mandel I., Broekgaarden F. S., 2022, *Living Reviews in Relativity*, 25, 1
- Maraschi L., Cavaliere A., 1977, *X-Ray Bursts of Nuclear Origin*. Springer Netherlands, Dordrecht, pp 127–128, doi:10.1007/978-94-010-1248-5_12, https://doi.org/10.1007/978-94-010-1248-5_12
- Mathews G. J., Wilson J. R., 1997, *ApJ*, 482, 929
- McDermott P. N., van Horn H. M., Hansen C. J., 1988, *ApJ*, 325, 725
- McWilliams S. T., Levin J., 2011, *ApJ*, 742, 90
- Meisel Z., Deibel A., Keek L., Shternin P., Elfritz J., 2018, *Journal of Physics G Nuclear Physics*, 45, 093001
- Metzger B. D., 2017, *Living Reviews in Relativity*, 20, 3
- Metzger B. D., 2019, *Living Reviews in Relativity*, 23, 1
- Metzger B. D., Fernández R., 2014, *MNRAS*, 441, 3444
- Metzger B. D., et al., 2010, *MNRAS*, 406, 2650
- Miralda-Escude J., Haensel P., Paczynski B., 1990, *ApJ*, 362, 572
- Mitidis A., 2015, PhD thesis, University of Florida
- Nicholl M., et al., 2017, *ApJ*, 848, L18
- Osborne E. L., Jones D. I., 2020, *MNRAS*, 494, 2839
- Papa M. A., et al., 2020, *ApJ*, 897, 22
- Passamonti A., Andersson N., 2012, *MNRAS*, 419, 638
- Passamonti A., Bruni M., Gualtieri L., Nagar A., Sopuerta C. F., 2006, *Phys. Rev. D*, 73, 084010
- Passamonti A., Andersson N., Pnigouras P., 2021, *MNRAS*, 504, 1273
- Peters P. C., 1964, *Physical Review*, 136, 1224
- Piro A. L., 2012, *ApJ*, 755, 80
- Piro A. L., Bildsten L., 2005, *ApJ*, 629, 438
- Press W. H., Teukolsky S. A., 1977, *ApJ*, 213, 183
- Press W. H., Vetterling W. T., Teukolsky S. A., Flannery B. P., 1986, *Numerical recipes*. Vol. 818, Cambridge university press Cambridge
- Prinsloo D., et al., 2018, in 12th European Conference on Antennas and Propagation (EuCAP 2018). pp 1–4
- Radice D., Perego A., Hotokezaka K., Fromm S. A., Bernuzzi S., Roberts L. F., 2018, *ApJ*, 869, 130
- Rajan R. T., Boonstra A.-J., Bentum M., Klein-Wolt M., Belien F., Arts M., Saks N., van der Veen A.-J., 2016, *Experimental Astronomy*, 41, 271
- Reisenegger A., Goldreich P., 1994, *ApJ*, 426, 688
- Robson T., Cornish N. J., Liu C., 2019, *Classical and Quantum Gravity*, 36, 105011
- Rosswog S., 2015, *International Journal of Modern Physics D*, 24, 1530012
- Roy P., Beri A., Bhattacharyya S., 2021, *MNRAS*, 508, 2123
- Saks N., Boonstra A.-J., Rajan R. T., Bentum M., Beliën F., van't Klooster K., 2010, in The 4S Symposium, Small Satellites Systems and Services.
- Samuelsson L., Andersson N., Maniopoulou A., 2007, *Classical and Quantum Gravity*, 24, 4147
- Saunders-Santos M., et al., 2017, *ApJ*, 848, L16
- Spitkovsky A., Levin Y., Ushomirsky G., 2002, *ApJ*, 566, 1018
- Sridhar N., Zrake J., Metzger B. D., Sironi L., Giannios D., 2021, *MNRAS*, 501, 3184
- Strohmayer T., Mahmoodifar S., 2014, *ApJ*, 793, L38
- Suvorov A. G., 2018, *MNRAS*, 478, 167
- Suvorov A. G., Kokkotas K. D., 2020, *Phys. Rev. D*, 101, 083002
- The LIGO Scientific Collaboration the Virgo Collaboration 2021, arXiv e-prints, p. arXiv:2108.01045
- The LIGO Scientific Collaboration the Virgo Collaboration the KAGRA Collaboration 2021a, arXiv e-prints, p. arXiv:2111.03606
- The LIGO Scientific Collaboration the Virgo Collaboration the KAGRA Collaboration 2021b, arXiv e-prints, p. arXiv:2111.03634
- The LIGO Scientific Collaboration the Virgo Collaboration the KAGRA Collaboration 2021c, arXiv e-prints, p. arXiv:2112.10990
- The LIGO Scientific Collaboration the Virgo Collaboration the KAGRA Collaboration 2022, arXiv e-prints, p. arXiv:2201.00697
- Tsang D., 2013, *ApJ*, 777, 103
- Tsang D., Read J. S., Hinderer T., Piro A. L., Bondarescu R., 2012, *Phys. Rev. Lett.*, 108, 011102

- Turner M., 1977a, [ApJ](#), **216**, 610
- Turner M., 1977b, [ApJ](#), **216**, 914
- Urpin V., 2004, [A&A](#), **421**, L5
- Ushomirsky G., Cutler C., Bildsten L., 2000, [Monthly Notices of the Royal Astronomical Society](#), 319, 902
- Vietri M., 1996, [ApJ](#), **471**, L95
- Wang L.-J., Tan L., Li Z., Misch G. W., Sun Y., 2021, arXiv e-prints, p. [arXiv:2102.06010](#)
- Wen D.-H., Li B.-A., Chen H.-Y., Zhang N.-B., 2019, [Phys. Rev. C](#), **99**, 045806
- Woosley S. E., Taam R. E., 1976, [Nature](#), **263**, 101
- Yakovlev D. G., Pethick C. J., 2004, [ARA&A](#), **42**, 169
- Yang H., East W. E., Paschalidis V., Pretorius F., Mendes R. F. P., 2018, [Phys. Rev. D](#), **98**, 044007
- Ye C. S., Fong W.-f., Kremer K., Rodriguez C. L., Chatterjee S., Fragione G., Rasio F. A., 2020, [ApJ](#), **888**, L10
- van Baal B. F. A., Chambers F. R. N., Watts A. L., 2020, [MNRAS](#), **496**, 2098